Supplementary Materials for

Omnidirectional Motion of an Untethered Tripodal Microrobot Using Radial Piezoelectric Actuators

Yu Gao[1]†, Jing Li[1]†, Shijing Zhang[1]†, Jipeng Yan[1], Yilin Zhang[1], Baoyi Liu[1], Jinghan Guan[1], Dehong Wang[1], Jie Deng[1]*, Yingxiang Liu[1]*

Affiliations:

[1]State Key Laboratory of Robotics and Systems, Harbin Institute of Technology, Harbin, 150001, China.

†These authors contributed equally to this work.

*Corresponding author. Email: liuyingxiang868@hit.edu.cn(Y.L.); dengjie21@hit.edu.cn (J.D.).

The PDF file includes:

Supplementary Table S1.

Other supplementary information for this manuscript includes the following:

Supplementary Movies 1 to 12.

Supplementary Movie 1: Mechanical configuration and working principle.
Supplementary Movie 2: Robot vibration mode test.
Supplementary Movie 3: Untethered locomotion characteristics of the tripodal robot.
Supplementary Movie 4: Robot performance across diverse substrates external loads, and slopes.
Supplementary Movie 5: Endurance test of the tripodal robot.
Supplementary Movie 6: Omnidirectional planar motion applications.
Supplementary Movie 7: The gas leak detection application demonstration.
Supplementary Movie 8: The microscopic observation applications.
Supplementary Movie 9: Cross-scale microscopic observation demonstration.
Supplementary Movie 10: Robot robustness evaluation.
Supplementary Movie 11: Demonstration of autonomous navigation.
Supplementary Movie 12: Multi-robot cooperative following demonstration.

Supplementary Note 1

Minimum reorientation cost

Due to operational requirements such as obstacle avoidance or task execution, the planar locomotion inevitably involves a sequence of reorientation processes. The 90° reorientation processes for both an omnidirectional robot and a robot with a finite turning radius are compared in Supplementary Fig. 1. Robots with a finite turning radius must adjust their orientation before moving toward the target, whereas omnidirectional robots can proceed directly to the target point. To quantitatively evaluate reorientation costs, we define a dimensionless metric termed the minimum reorientation cost (RC_{min}), representing the cost incurred by the robot during a single reorientation of π/2. We define A_{body} as the area of the maximum circumscribed circle of the robot's vertical projection onto the plane. Consequently, the RC_{min} is defined as the ratio of the minimum area swept by A_{body} (denoted as A_{swept}) during a single reorientation of π/2 to A_{body} itself. That is:

$$RC_{min} = \frac{A_{swept}}{A_{body}} = \frac{A_{swept}}{\pi R_{max}^{2}} \quad (1)$$

Where R_{max} is the radius of the maximum circumscribed circle of the robot's planar projection (Unit: mm).

For omnidirectional robots (OM robots), the transition from a forward heading to a lateral leftward trajectory involves no attitude adjustment and is achieved solely by altering the drive signals (see Supplementary Fig. 1a). Consequently, the area swept during reorientation remains A_{body}, yielding an RC_{min} of 1.

$$\mathrm{RC}_{\min}^{\mathrm{OM}} = 1 \tag{2}$$

For a robot with a finite turning radius (TR robots), motion is constrained by a turning radius r_{turn} (assuming a constant radius during the steering maneuver). The reorientation process is illustrated in Supplementary Fig. 1b. Consequently, the $\mathrm{RC}_{\min}$ is given by:

$$\mathrm{RC}_{\min}^{\mathrm{TR}} = \frac{\frac{\pi/2}{2}[(r_{\mathrm{turn}} + R_{\max})^2 - (r_{\mathrm{turn}} - R_{\max})^2] + \pi {R_{\max}}^2}{\pi {R_{\max}}^2} = 1 + \frac{r_{\mathrm{turn}}}{R_{\max}} \tag{3}$$

In conclusion, the ranking of $\mathrm{RC}_{\min}$ for the two robot categories is:

$$\mathrm{RC}_{\min}^{\mathrm{OM}} < \mathrm{RC}_{\min}^{\mathrm{TR}} \tag{4}$$

Thus, the omnidirectional motion robot exhibits the lowest reorientation cost, while the TR robot incurs the higher cost. This advantage affords the OM robot better traversability in narrow spaces and reduced control overhead. The simplification of control logic is particularly critical in scenarios involving high-frequency, computationally intensive operations, such as closed-loop navigation and path planning. Admittedly, this cost estimation method implies certain limitations. For instance, it primarily focuses on the angular cost associated with the robot's self-reorientation, while the operational energy expenditure throughout the entire trajectory and the computational complexity of the actual motion algorithms are not fully accounted for.

Supplementary Note 2

Principle of the interpolation locomotion algorithm

The robot motion strategy includes two key approaches, including the tripodal radial actuation strategy (Approach 1) and trajectory interpolation algorithm (Approach 2). Approach 1 offers six selectable directions, as shown in Supplementary Fig. 4a. The angle between the central axes of any two adjacent combinations (envelope angle) is 60°. The straight line connecting the robot's current position and the target point lies within the envelope angle formed by two adjacent combinations, which are then selected as the basis vectors (actuation combinations) for the interpolation algorithm. If the connecting line happens to coincide with one of the basis vectors, that vector is directly chosen as the next actuation combination. We define the interpolation reference angle Θ as the angle between this connecting line and the robot's leg-2. The upper basis vector A with respect to the connecting line will cause Θ to increase, while the lower basis vector B will cause Θ to decrease. Utilizing this characteristic, the robot decomposes and densifies the original straight path into the two basis vectors and ultimately reaches the target point.

We present an example of the locomotion process, as shown in Supplementary Fig. 4b. The red point represents the robot's current position, while the blue point indicates the target point to be reached. The black dashed line denotes the shortest trajectory, and the green line represents the actual locomotion path. Based on the coordinates of the red current position and the blue target point, the robot determines two basis actuation combinations: Combination A (leg-2 and leg-3) and Combination B (leg-3). In the selected configuration (Combination A or Combination B), the actuation unit in the combination operates in the optimal vibration state (OVS), whereas the unit outside of the combination functions in the low-frequency bounce state (LBS). These two combinations serve as the basis vectors for the interpolation algorithm.

The robot first moves in the direction of combination B, during which the interpolation angle Θ gradually decreases. Once Θ reaches a predefined threshold, the actuation switches to combination A, and the robot continues moving, now with Θ gradually increasing. This alternating process is repeated until the robot successfully reaches the target point. The threshold of the interpolation angle Θ is determined by the densification level of the interpolated trajectory. A higher densification level results in a smaller allowable variation range for Θ and a higher frequency of switching between the basis vectors. The above discussion considers the case where the robot undergoes no body deflection. Although the robot have no rotational degrees of freedom, unavoidable attitude deviations may occur during its motion. The deflection angle is defined by the yaw angle, which can be recorded in real time by an onboard attitude sensor, as shown in Supplementary Fig. 4c. After deflection, the robot requires compensation of the yaw angle based on the original interpolation reference angle Θ, as shown in Supplementary Fig. 4d.

Supplementary Note 3

Material properties of the robot

The robot prototype is completed by computer numerical control (CNC) machining and laser cutting, and the material is aluminum alloy (2A12, Density of 2.77×10^3 kg/m^3, Young's modulus of 7.1×10^{10} N/m^2, and Poisson's ratio of 0.33). The piezoelectric ceramic plates are made of PZT-4 (Lead Zirconate Titanate, Density of 7.6×10^3 kg/m^3). The main component of the driving foot is alumina (Density of 3.9×10^3 kg/m^3, Young's modulus of 3×10^{11} N/m^2, and Poisson's ratio of 0.22). Other physical parameters of PZT-4 obtained from the supplier are as follows:

$$[C]=\begin{bmatrix} 14.3 & 7.85 & 7.85 & 0 & 0 & 0 \\ 7.85 & 14.3 & 7.85 & 0 & 0 & 0 \\ 7.85 & 7.85 & 11.5 & 0 & 0 & 0 \\ 0 & 0 & 0 & 2.45 & 0 & 0 \\ 0 & 0 & 0 & 0 & 2.6 & 0 \\ 0 & 0 & 0 & 0 & 0 & 2.6 \end{bmatrix}\times10^{10}\ \text{N/m}^2 \tag{5}$$

$$[e]=\begin{bmatrix} 0 & 0 & -2.4 \\ 0 & 0 & -2.4 \\ 0 & 0 & 17.3 \\ 0 & 0 & 0 \\ 0 & 12.95 & 0 \\ 12.95 & 0 & 0 \end{bmatrix}\ \text{C/m}^2 \tag{6}$$

$$[\varepsilon]=\begin{bmatrix} 765 & 0 & 0 \\ 0 & 765 & 0 \\ 0 & 0 & 640 \end{bmatrix}\times10^{-11}\ \text{F/m} \tag{7}$$

Where $[C]$, $[e]$ and $[\varepsilon]$ are the stiffness matrix, the piezoelectric matrix, and the dielectric matrix, respectively.

Supplementary Note 4

Determination process of the key structural parameters.

Based on the three influencing factors for determining actuation unit parameters summarized in the main manuscript, we conduct a series of simulation analyses. Considering the available sizes of piezoelectric ceramics in the laboratory and the miniaturization requirement of the robot, the overall size of the robot are determined. The key component affecting the robot's performance is the thin plate, which directly influences both the stability of the mode and the foot-end displacement of the actuation unit. The two critical structural parameters of the thin plate are its thickness and height, as shown in Supplementary Fig. 6a. Note: the coordinate system of the actuation unit is defined according to Supplementary Fig. 6a. This applies to both the transient dynamics simulation and the vibration displacement tests of the driving foot.

Firstly, we use the frequency difference of the first-order bending mode frequency of the robot (in its non-driving-foot version) to evaluate the stability of the mode. A larger frequency difference indicates more distinct mode separation in the first-order bending mode, reflecting less stability. The simulation results for different thickness and height combinations are shown in Supplementary Fig. 6b. The results show that a larger height and a thinner thin plate lead to a smaller modal extremum, which represents better modal merging results.

Moreover, excessively increasing the height of the thin plate would result in an oversized robot, while decreasing the height too much would limit the available thickness range. For example, when the height is set to 3 mm, the modal frequency extremum starts to increase rapidly when the thickness exceeds 0.35 mm (reflected by the transition from purple to blue regions in the heatmap, difference > 50). Therefore, we ultimately chose a thin plate height of 4 mm.

Secondly, the thickness of the thin plate plays an important role in determining the foot-end displacement of the actuation unit. We conduct harmonic response simulations to evaluate the foot-end displacement under different thicknesses, as shown in Supplementary Fig. 6c. The results indicate that increasing the plate thickness leads to a decrease in foot-end displacement, which negatively affects the output driving force. However, an excessively thin plate can cause fabrication challenges and compromise size stability. Considering both performance and manufacturability, a thickness of 0.4 mm is selected. At this thickness, the extremum of the first-order bending mode frequency is 17, and the simulated foot-end displacements in the OZ and OY directions are 8.16 μm and 10.74 μm, respectively. (Note: Although harmonic response analysis may differ slightly from transient simulation results, the discrepancy is minor. Given its computational efficiency, harmonic response analysis is used during parameter selection, while transient analysis is used to confirm the final results.)

Supplementary Note 5

Motion efficacy analysis

The power consumption of the tethered tripodal robot is characterized using a digital power meter (WT210, Yokogawa, Japan). Supplementary Fig. 8a illustrates the power consumption of a single driving leg as a function of excitation voltage in both OVS and LBS. At a constant frequency, the power consumption of the driving leg correlates positively with the applied voltage. Specifically, the maximum power consumption in LBS is measured at 313.8 mW (60 $V_{p\text{-}p}$). At an operating voltage of 30 $V_{p\text{-}p}$, the power consumption for OVS and LBS is 154.3 mW and 74.0 mW, respectively. The resultant locomotion direction of the proposed tripodal robot is determined by the vector synthesis of the propulsive forces generated by the three driving legs (Supplementary Fig. 8b). The motion coordination is categorized into two modes:

- Single actuation mode (Supplementary Fig. 8b(i)):

Two driving legs are configured in LBS, while one leg serves as the primary actuator in OVS. Since the LBS is a friction-reduction mode, its driving force is assumed to be negligible (indicated by green dashed circles), whereas the leg in OVS provides the effective propulsive force (indicated by the blue arrow).

- Dual actuation mode (Supplementary Fig. 8b(ii)):

The robot's heading is determined by the resultant vector of two legs operating in OVS. Under the assumption of equal driving forces from both OVS legs, the motion direction bisects the angle between them. For locomotion in arbitrary directions, the heading is synthesized by modulating the ratio of the driving force magnitudes between the two legs in OVS.

As shown in Supplementary Fig. 8c, the robot's workspace is divided into six symmetrical sectors. The global coordinate system is defined by aligning the X-axis with the longitudinal axis of leg #1. The locomotion heading, defined by the yaw angle θ in [0°, 360°), is measured counter-clockwise from the positive X-axis. Taking the motion direction within the first sector (θ in [0°, 60°)) as an example (indicated by the red arrow in Supplementary Fig. 8c), the steering strategy is implemented as follows:

- Main leg: Leg #1 operates at full power as the primary propulsion source, with its normalized output force defined as $u_1 = 1$.
- Auxiliary leg: Leg #2 serves as an auxiliary actuator, providing a modulated driving force with a normalized coefficient $u_2 = K(\theta)$.
- Friction-reduction leg: Leg #3 is set to the LBS state, contributing negligible propulsive force $u_3 = 0$.

Based on the Law of Sines within the force vector triangle, the relationship between the required yaw angle θ and the driving coefficient $K(\theta)$ of the auxiliary leg can be derived. To synthesize a resultant motion at angle θ, the coefficient $K(\theta)$ is determined by:

$$K(\theta) = \frac{\sin(\theta)}{\sin(120° - \theta)}, \quad \theta \in \left[0°, 120°\right) \tag{8}$$

The modulation coefficient $K(\theta)$ is constrained within the range [0, 1]. This coefficient facilitates a seamless transition between the two previously defined actuation modes: when $\theta = 0°$, $K = 0$ (corresponding to single actuation mode), and when $\theta = 60°$, $K = 1$ (corresponding to dual actuation mode). Taking the 30 $V_{p\text{-}p}$ excitation voltage as a representative case, we assume that the effective propulsive force is linearly proportional to the electrical power consumed for mechanical work. Based on the experimental data, the power consumption model for a single driving leg can be formulated as follows:

$$P_{\text{leg}}(u) = \begin{cases} P_{\text{LBS}}, & u \approx 0 \\ P_{\text{LBS}} + u \cdot (P_{\text{OVS}} - P_{\text{LBS}}), & 0 < u \leq 1 \end{cases} \tag{9}$$

The power consumption of an individual driving leg, denoted as $P_{\text{leg}}(u)$, is modeled as a function of the control coefficient u. For a constant excitation voltage of 30 $V_{p\text{-}p}$, let P_{LBS} represent the power consumption in LBS (74.0mW) and P_{OVS} represent the power consumption in OVS (154.3 mW).

It can be inferred from the aforementioned model that the robot incurs a baseline power cost, defined by P_{LBS}, even when no effective propulsive force is generated. This baseline represents the essential energetic cost of maintaining the friction-reduction state. The total system power consumption, P_{total}, is calculated as the scalar summation of the power dissipated by the three independent driving legs:

$$P_{\text{total}}(\theta) = \sum_{i=1}^{3} P_{\text{leg}}(u_i) = P_{\text{OVS}} + 2P_{\text{LBS}} + (P_{\text{OVS}} - P_{\text{LBS}}) \cdot K(\theta) \tag{10}$$

While the preceding analysis focuses on the first sector, the methodology remains consistent across all six motion sectors by adjusting the range of the yaw angle θ and the assignment of the driving coefficient $K(\theta)$ to the respective auxiliary legs. Supplementary Fig. 8d provides a comprehensive summary of the target angles, driving coefficients, and the corresponding operational states of each leg across all sectors.

To evaluate the energetic cost of different locomotion strategies at 30 $V_{p\text{-}p}$, we compare the two primary actuation modes:

- For the single actuation mode ($\theta = 0°$, $K = 0$), the total power consumption is calculated as:

$$P_{\text{total}} = P_{\text{OVS}} + 2P_{\text{LBS}} \approx 302.3 \text{ mW} \tag{11}$$

- For the dual actuation mode ($\theta = 60°$, $K = 1$), the total power consumption is calculated as:

$$P_{\text{total}} = 2P_{\text{OVS}} + P_{\text{LBS}} \approx 382.6 \text{ mW} \tag{12}$$

The power consumption in the dual actuation mode is approximately 1.27 times that of the single actuation mode. For force characterization, we normalize the resultant driving force based on the output of a single leg in the single actuation mode ($\theta = 0°$). Under this benchmark, only Leg #1 generates propulsive force. Consequently, the normalized magnitude of the synthesized resultant force, $\left|F_{\text{syn}}(\theta)\right|_{\text{norm}}$, is determined by the following vector summation:

$$\begin{aligned} \left|F_{\text{syn}}(\theta)\right|_{\text{norm}} &= \sqrt{1 + K(\theta)^2 + 2K(\theta)\cos(120°)} \\ &= \sqrt{1 - K(\theta) + K(\theta)^2} \end{aligned} \tag{13}$$

The normalized driving force coefficient across the full 0° ~ 360° range is shown in Supplementary Fig. 8e. The analysis reveals that the resultant driving force reaches its local maxima at the three fundamental actuation directions and the three primary symmetric synthesis directions. Conversely, the minimum driving force coefficient (approximately 0.87) occurs at the six offset synthesis angles (e.g., 30°). Similarly, Supplementary Fig. 8f presents the total power consumption, normalized to the baseline power of the single actuation mode at $\theta = 0°$. Within each sector, the power consumption exhibits an approximately linear relationship with the yaw angle. The normalized power consumption coefficient reaches its peak of 1.27 at the dual-leg synthesis directions.

To quantitatively evaluate the trade-off between propulsive output and energetic investment across different headings, we define a dimensionless parameter, motion efficacy ($\eta(\theta)$), expressed as:

$$\eta(\theta) = \frac{\left|F_{\text{syn}}(\theta)\right|_{\text{norm}}}{P_{\text{total}}(\theta)_{\text{norm}}} \tag{14}$$

The motion efficacy of the robot across different headings is illustrated in Supplementary Fig. 8g. The results indicate that the robot achieves its peak locomotion efficacy at the three fundamental directions (i.e., 0°, 120°, and 240°), where only a single leg operates in OVS. In the dual actuation mode (e.g., 60°), the efficacy factor drops to 0.79 due to the increased power demand of concurrent leg activation. Furthermore, the efficacy reaches its minimum of approximately 0.75 at the offset synthesis angles, such as in the vicinity of 40° and 80°. This degradation in motion efficacy at synthesis angles can be attributed to the geometric projection loss inherent in vector summation. In the dual actuation mode and its adjacent offset angles, a portion of the generated driving force from each active leg is neutralized through internal cancellation along the non-target axes, whereas the total electrical power consumption scales cumulatively with the number of active actuators. Consequently, the rate of increase in power demand exceeds the growth of the resultant propulsive force, leading to a diminished efficacy profile compared to the single-leg actuation at fundamental angles.

It is worth noting that the motion efficacy model presented here, developed using the 30 V_{p-p} case as a benchmark, incorporates several simplifying assumptions. Specifically, the model assumes a linear proportionality between the electrical power consumption and the resultant mechanical thrust, while neglecting potential non-linear effects such as interfacial friction heat dissipation, complex leg-ground interactions, and phase-dependent interference between multiple actuators.

Supplementary Note 6

Design of the onboard circuit unit

The working principle of the actuation part in the onboard circuit unit is shown in Supplementary Fig. 8a. The circuit board can achieve three independent signal outputs, with a maximum output voltage of 60 $V_{p\text{-}p}$. The schematic diagram of the circuit board is shown in Supplementary Fig. 8b. Specifically, positive high voltages are generated by two single-chip high-frequency switching regulators and transformers, which are provided to the boost circuit (Supplementary Fig. 8b(i)). The negative voltage generation circuit uses the charge pump principle and the low-noise regulated inverter chip to generate a negative voltage, which serves as the negative power supply input for the amplifier (Supplementary Fig. 8b(ii)). The high voltage operational amplifier is configured as a comparator to generate a corresponding high frequency output (Supplementary Fig. 8b(iii)). All power is supplied to each module by a 180 mAh lithium battery (Supplementary Fig. 8b(iv)). The control chip is ESP32-PICO-D4 (Espressif, China), which provides communication and control signals (Supplementary Fig. 8b(v)). The control chip and high-temperature components, such as transformers, are arranged on the outside of the circuit board to dissipate the operating heat.

Supplementary Note 7

CoT evaluation of the robot

The cost of transport (CoT) is commonly used in biology to assess the locomotion cost of insects and is also employed for evaluating the motion energy consumption of robots. It is determined by the following formula:

$$\text{CoT}=\frac{P}{mgv} \tag{1}$$

where P is the instantaneous power consumption, m is the weight of the robot, g is the gravitational acceleration, and v is the robot speed. We utilize a digital power meter (WT210, Japan) to measure the power consumption of the robot with the onboard circuit unit (60 $V_{p\text{-}p}$). The corresponding locomotion speed of the robot is 30.08 mm/s. The power consumption of the robot is 0.5 W. Thus, the CoT reaches 139. We conduct a simple comparison with the CoT of similar miniature robots and insects, as shown in Supplementary Fig. 17. Note: the partly CoT values are not explicitly published in the papers. They are calculated to the best of our ability using the available data. The results show that the robot achieves a good balance between high integration and power consumption. However, due to size and weight limitations, the low actuation power of the onboard circuit unit may have a negative effect on the motion effect of the robot.

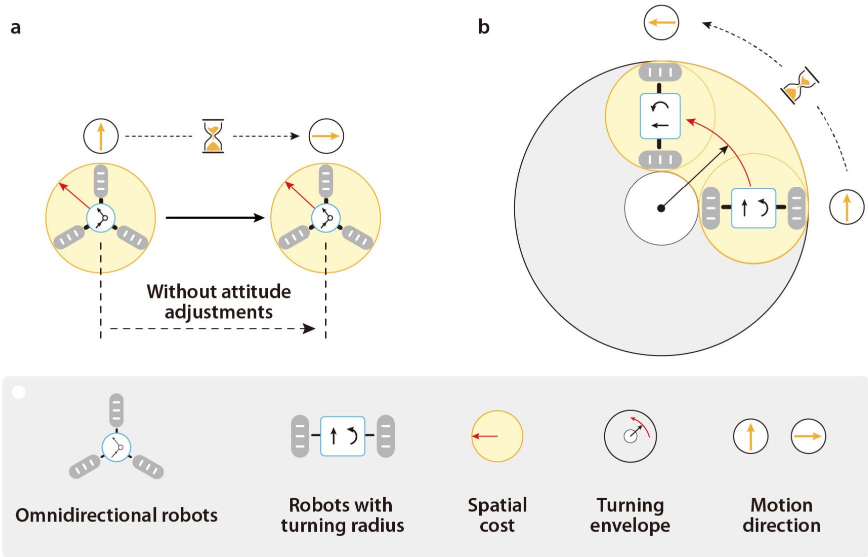

Supplementary Fig. 1.

The calculation of the minimum reorientation cost. (a) RC_{min} of the omnidirectional robots. **(b)** RC_{min} of the robots with turning radius.

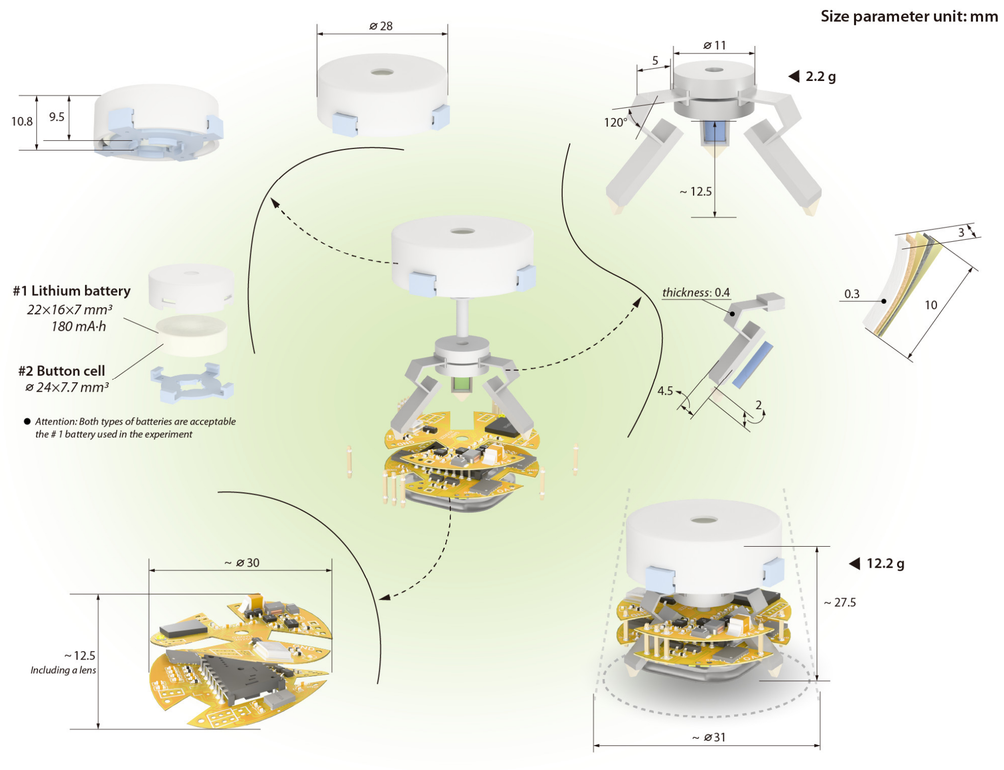

Supplementary Fig. 2.

The key structural parameters and weight of each unit.

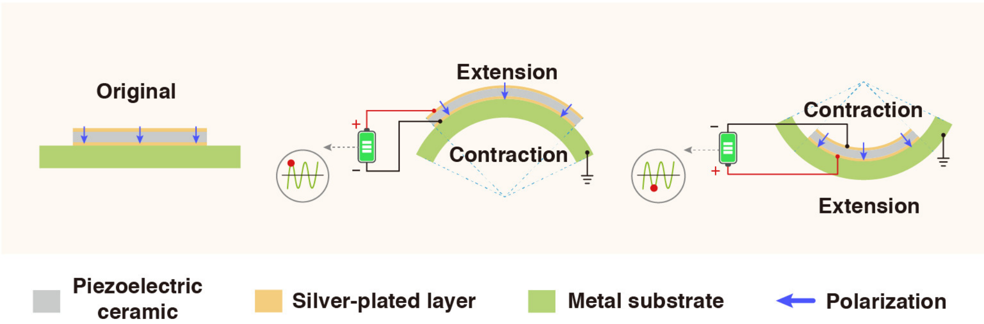

Supplementary Fig. 3.

Actuation mechanism of piezoelectric ceramics.

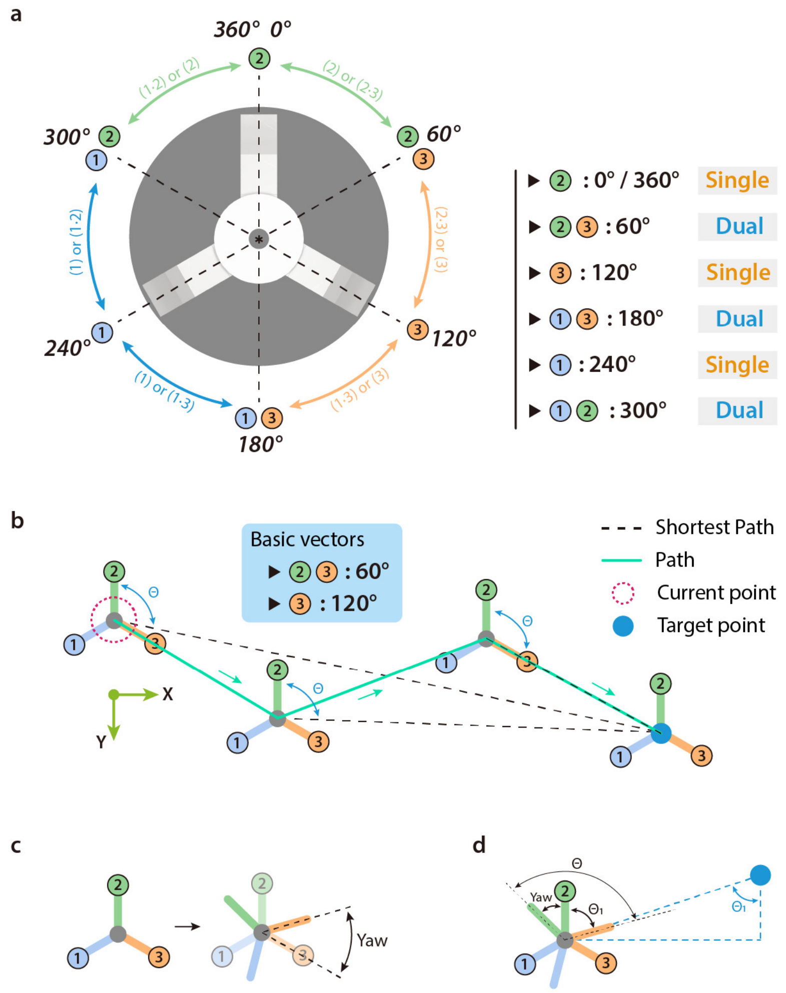

Supplementary Fig. 4.

The interpolation locomotion algorithm. **(a)** The six basis vectors of the robot. **(b)** An interpolation motion example. **(c)** The case of robot attitude deviation. **(d)** Corrected interpolation reference angle.

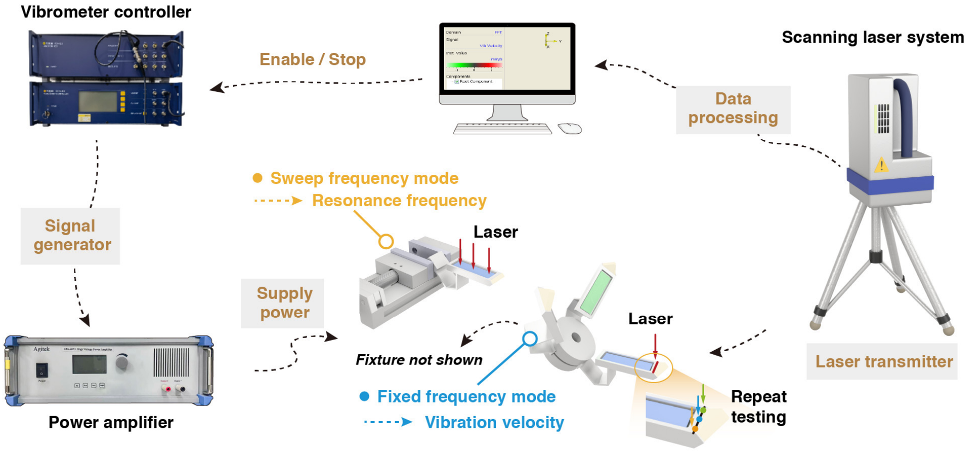

Supplementary Fig. 5.

Laser vibration measurement platform. Note: The system operates in two modes: sweep frequency mode and fixed frequency mode. By default, a 10 $V_{p\text{-}p}$ excitation voltage is applied to the actuation units during testing.

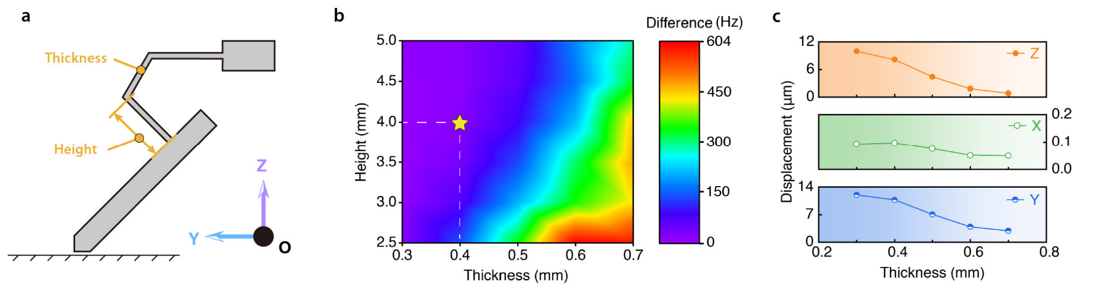

Supplementary Fig. 6.

Actuation unit parameter determination and simulation results. (a) Key parameters: thickness and height. **(b)** Parametric variations in height and thickness influence the frequency difference of the first-order bending vibration mode in the actuation unit. **(c)** Relationship between the thickness of the thin plate and the foot-end displacement of the actuation unit (harmonic response simulations).

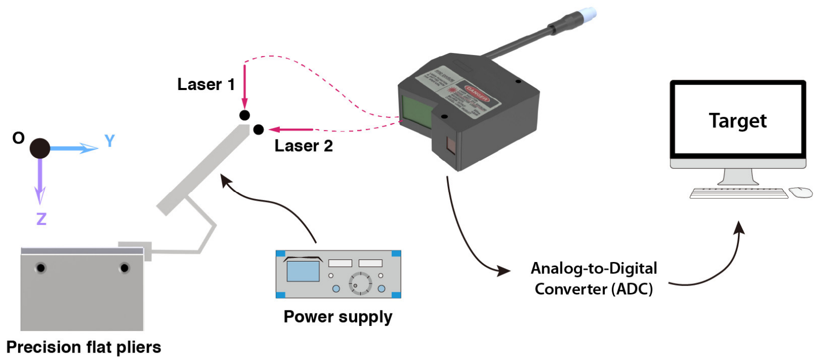

Supplementary Fig. 7.

Micro-displacement measurement platform.

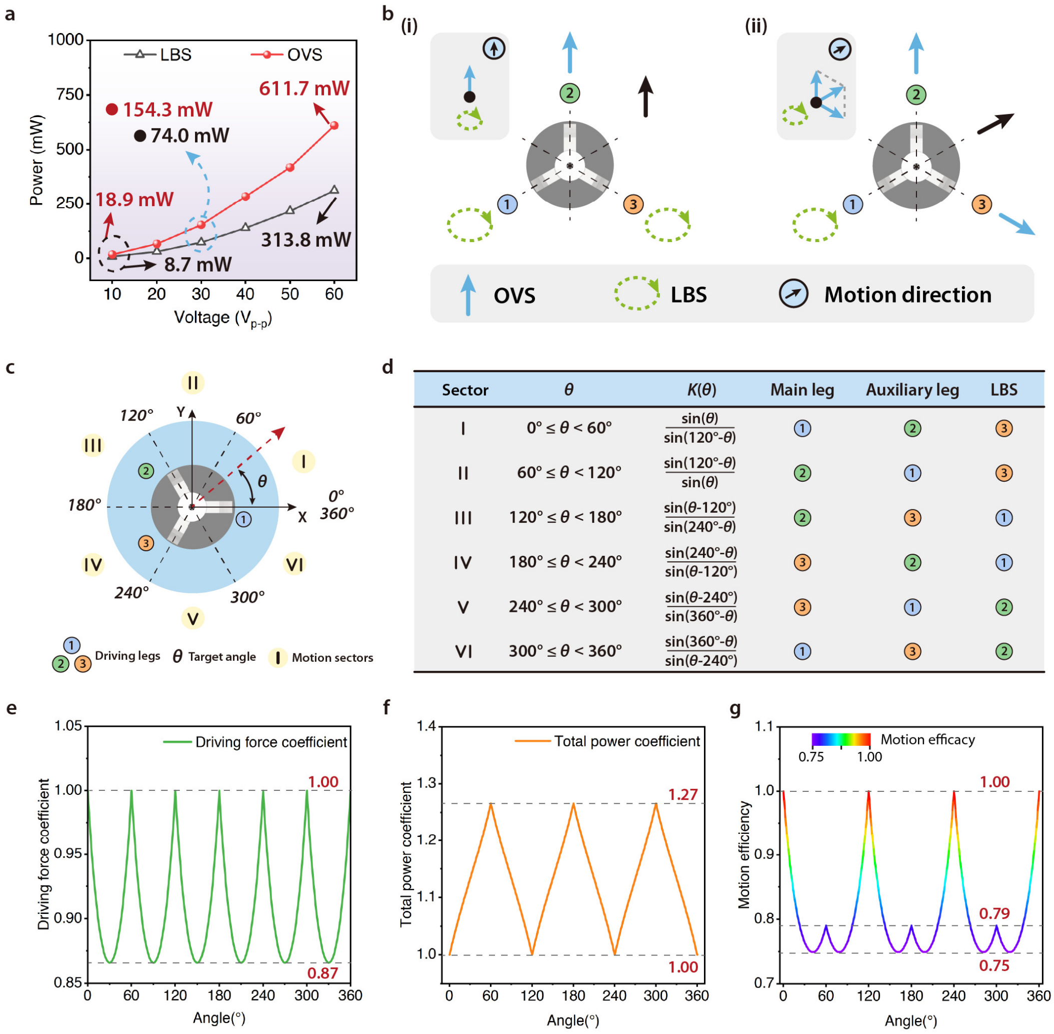

Supplementary Fig. 8.

Motion efficacy analysis of the robot. (a) Power consumption of the driving leg as a function of voltage under different modes (OVS and LBS). **(b)** Schematic of the driving leg states and resultant force synthesis in two actuation modes. **(c)** Definition of the coordinate frames and sectors in the robot's motion efficacy model. **(d)** Summary of target angles (θ), driving coefficients ($K(\theta)$), and the corresponding states of different legs across various motion sectors. **(e)** Normalized driving force coefficient across the 0° ~ 360° range of motion directions (normalized to the driving force at a 0° motion angle in single actuation mode). **(f)** Normalized total power consumption coefficient across the 0° ~ 360° range of motion directions (normalized to the power consumption at a 0° motion angle in single actuation mode). **(g)** Motion efficacy of the robot across different motion directions from 0° ~ 360°.

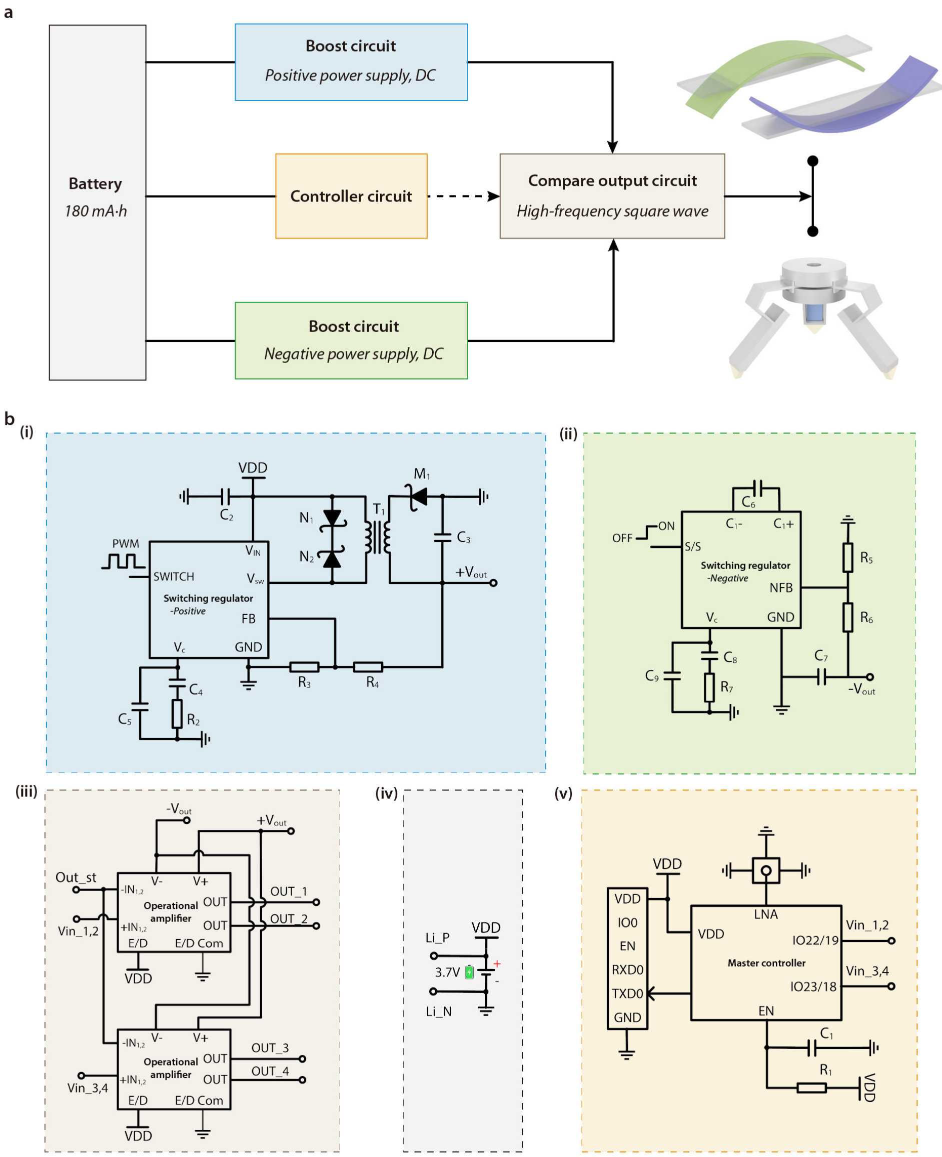

Supplementary Fig. 9.

Framework and circuit schematic of the onboard circuit unit. (a) Working principle. **(b)** The circuit schematic diagram. (i) Positive voltage boost output circuit. (ii) Negative voltage boost output circuit. (iii) Operational amplifier output circuit. (iv) Power supply circuit. (v) Main control chip and peripheral circuit.

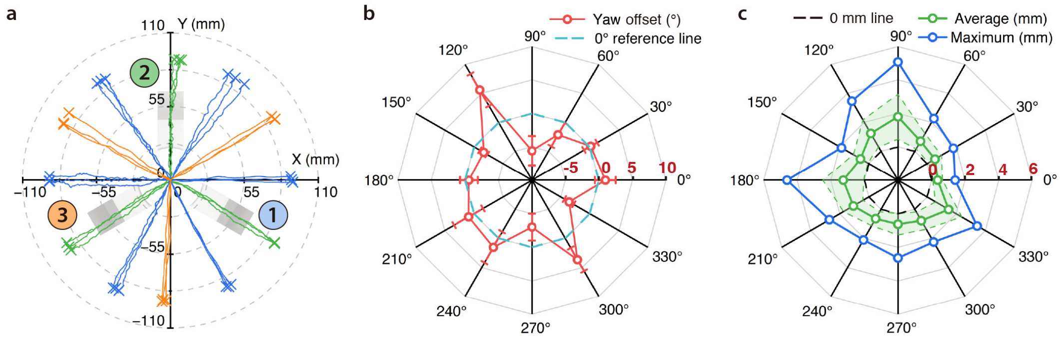

Supplementary Fig. 10.

Demonstration and evaluation of planar motion across twelve discrete directions. **(a)** Trajectory map of the robot across 12 directions with 30° increments (each movement spans 90 mm; three trials per direction). **(b)** Yaw offset across different motion directions. The yaw angle is defined as the orientation of the motion trajectory relative to the positive x-axis (ranging from 0° to 360°), and the offset represents the angular difference between the actual trajectory and the theoretical target angle. Minimum value: offset 0.2° at 30°, maximum value: offset 5.6° at 120°. The error bars indicate the standard deviation for n = 3 sample measurements at each data point. **(c)** Evaluation of trajectory deviations across motion directions. For a 90-mm trajectory segment, the average deviation ranges from a minimum of 0.4 mm (0.4% relative to travel distance) at 0° to a maximum of 1.8 mm (2.0%) at 90°. The maximum deviation ranges from a minimum of 1.4 mm (1.6%) at 0° to a maximum of 5.1 mm (5.7%) at 90°. The green dashed area represents the standard deviation for n = 3 sample measurements at each data point. Note: Data obtained from a representative prototype (Prototype #2). Deviation metrics: Trajectory precision is quantified by the average deviation ($D_{\text{avg}} = \frac{1}{n}\sum|d_i|$) and maximum deviation ($D_{\max} = \max|d_i|$). Here, d_i represents the perpendicular distance of each actual trajectory point from the straight line connecting the segment's start and end points.

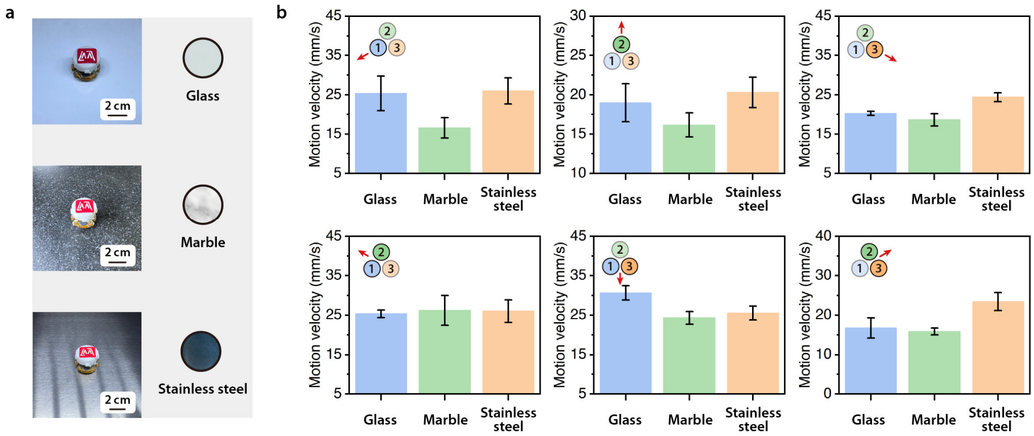

Supplementary Fig. 11.

Performance of the robot on diverse contact substrates. (a) Photographs of the robot situated on glass, marble, and stainless-steel surfaces. **(b)** The velocity characteristics across six motion directions on the three respective substrates. The robot achieves a peak velocity of 30.66 mm/s on the glass substrate (actuation: #1 and #3; LBS: #2). In comparison, the maximum locomotion speeds on marble and stainless-steel surfaces reach 26.21 mm/s and 26.06 mm/s, respectively (actuation: #1 and #2; LBS: #3 for both cases). Note: Data obtained from a representative prototype (Prototype #2, 60 $V_{p\text{-}p}$). The error bars indicate the standard deviation for n = 3 sample measurements at each data point.

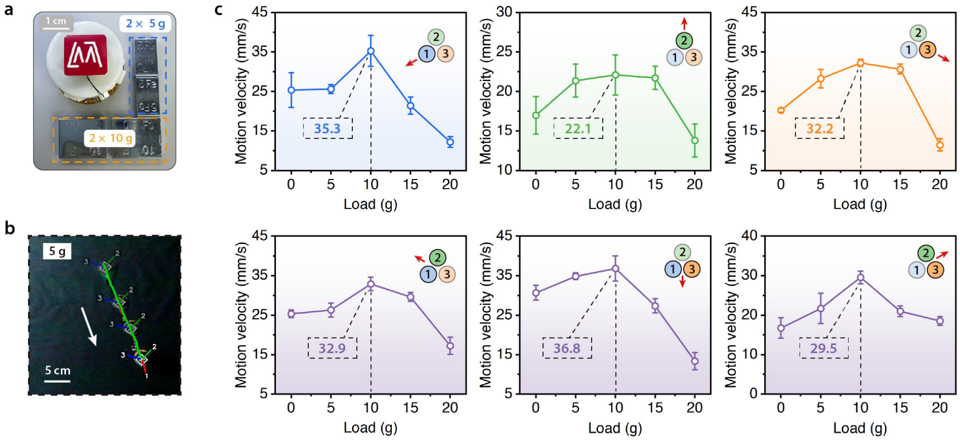

Supplementary Fig. 12.

Payload capacity and locomotion characterization. (a) Photographs of the robot and the standard weights used for testing (5 g and 10 g). **(b)** Time-lapse stacked images showing the robot performing locomotion with a 5 g payload. **(c)** Locomotion velocity as a function of the applied payload. The robot sustains a maximum additional payload of 20 g. Considering the onboard electronics and battery (10 g), the total carried load reaches 30 g, which is approximately 13.63 times the robot's body weight (the mass of the tripodal robot is 2.2 g). Note: Data obtained from a representative prototype (Prototype #2, 60 $V_{p\text{-}p}$). The error bars indicate the standard deviation for n = 3 sample measurements at each data point.

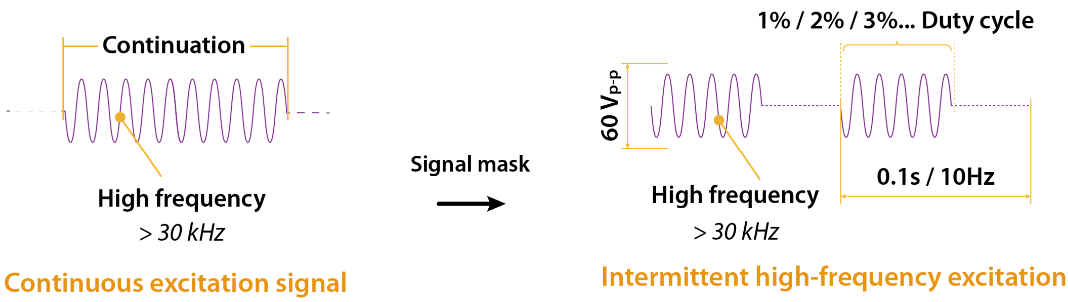

Supplementary Fig. 13.

Intermittent excitation signals generated by applying a signal mask.

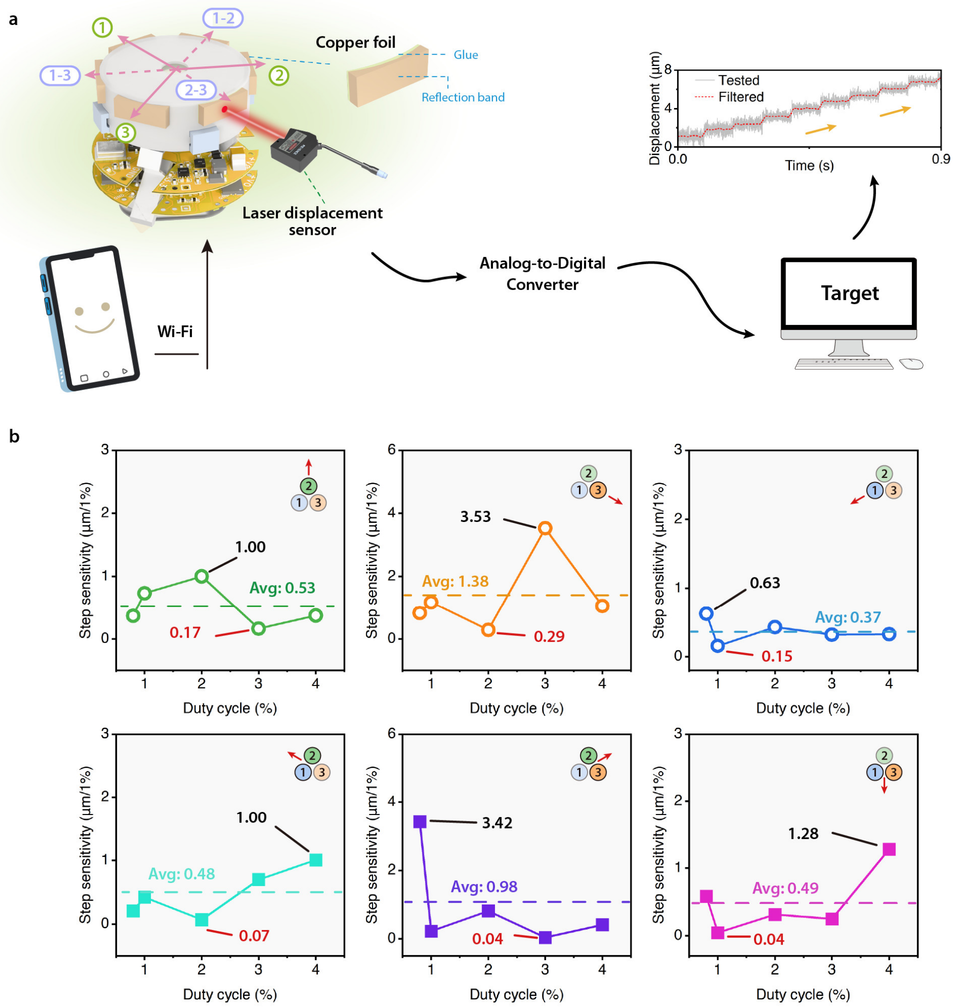

Supplementary Fig. 14.

Microscopic step motion testing platform and step sensitivity evaluation. (a) Schematic of the system. **(b)** Step sensitivity in six basic directions. Note: this metric is used to quantify the variation rate of the robot's step size, expressed as the amount of step-size change per 1% duty-cycle increment.

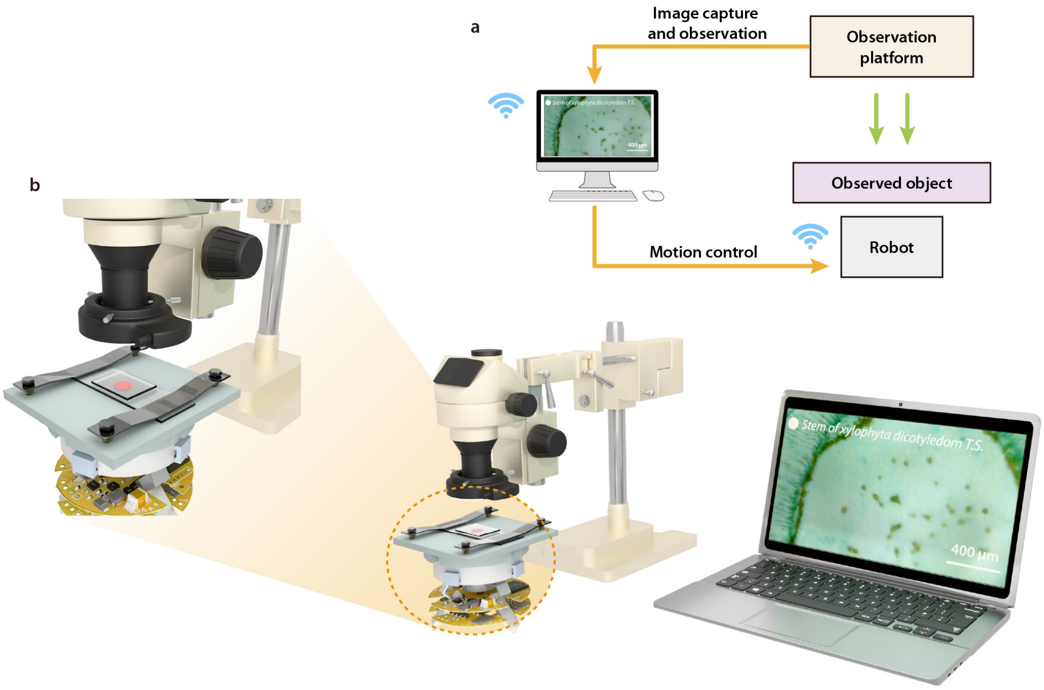

Supplementary Fig. 15.

Microscopic observation platform. (a) Schematic of the system. **(b)** The platform consists of a high-magnification microscope, the robot, an object stage, and a host computer.

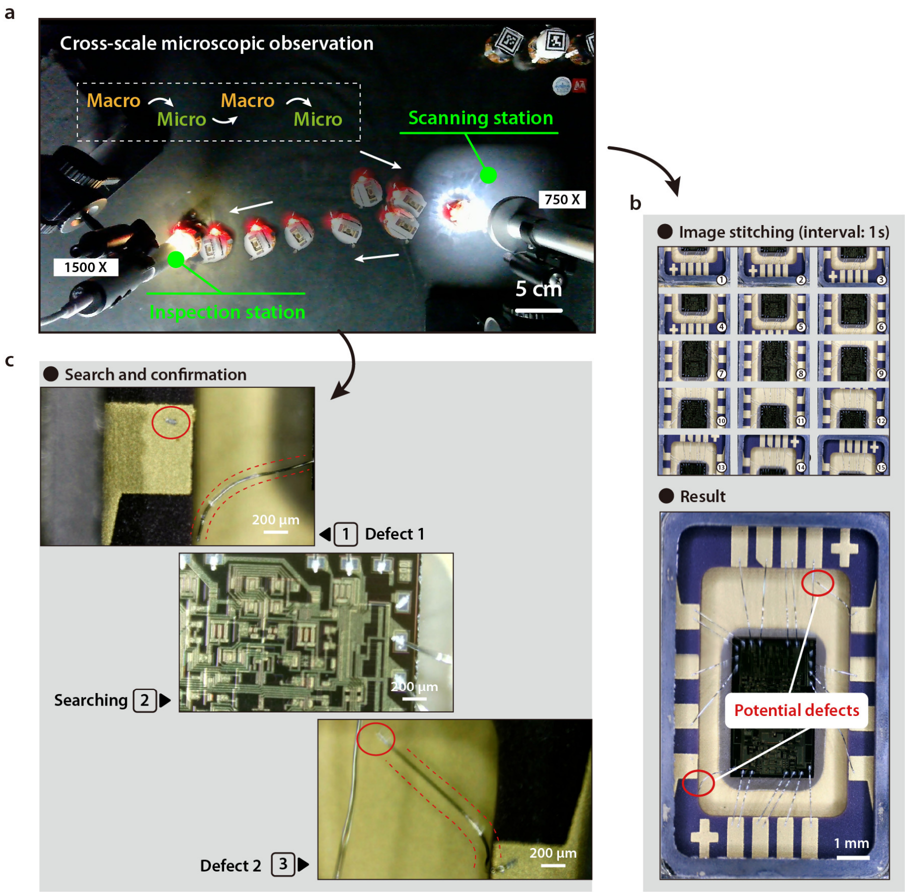

Supplementary Fig. 16.

Cross-scale microscopic observation application. (a) Global camera view for cross-scale operation. The robot moves to the scanning station, where it utilizes its high-precision stepping mode to perform image stitching of a target chip. Then it switches to fast macroscopic locomotion to reach the inspection station for detailed defect localization. **(b)** Raw sequential frames (interval: 1 s) and the stitched result. Two potential defects (Suspected breakage and detachment of bonding wire) are identified within the stitched panoramic image. **(c)** Defect search and identification. Detailed localization and confirmation of the two identified defects are performed at the inspection station.

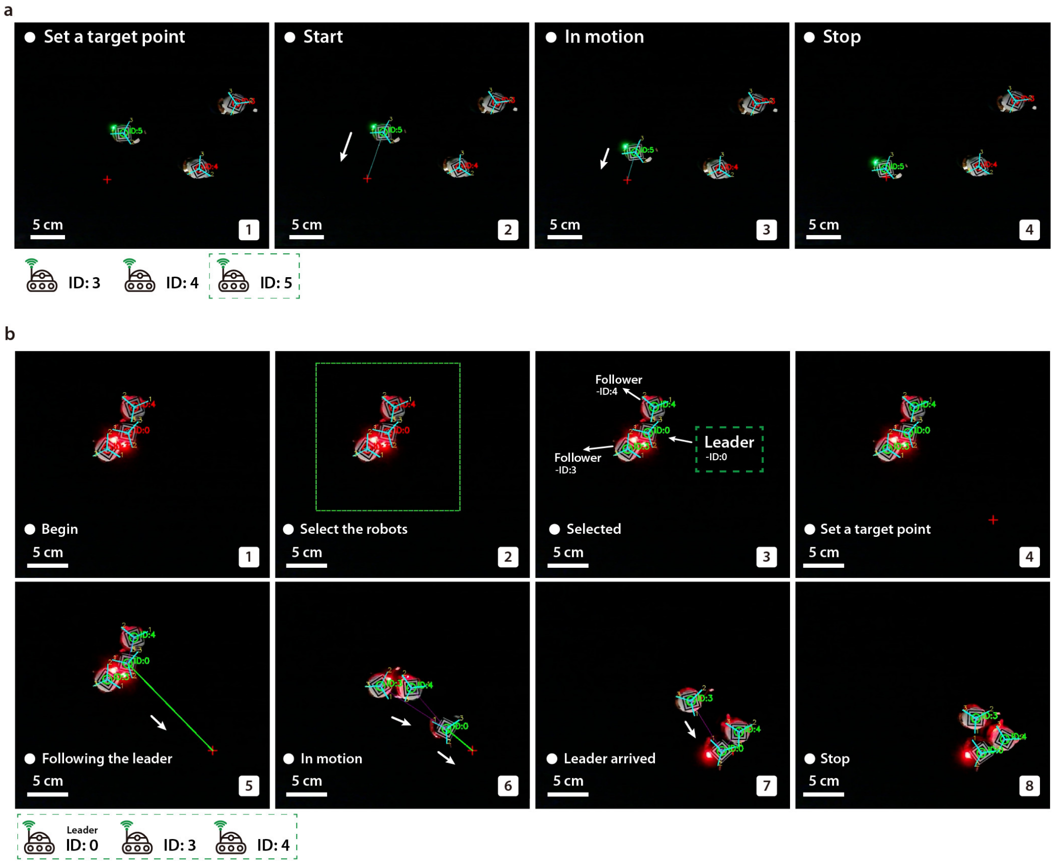

Supplementary Fig. 17.

The PTP navigation system for multi-robot following applications. (a) Users can control the motion of a single robot through the interactive interface of the video stream based on the robot vision feedback platform. **(b)** Two follower robots track the leader robot (ID: 0) to achieve coordinated motion using the PTP navigation algorithm.

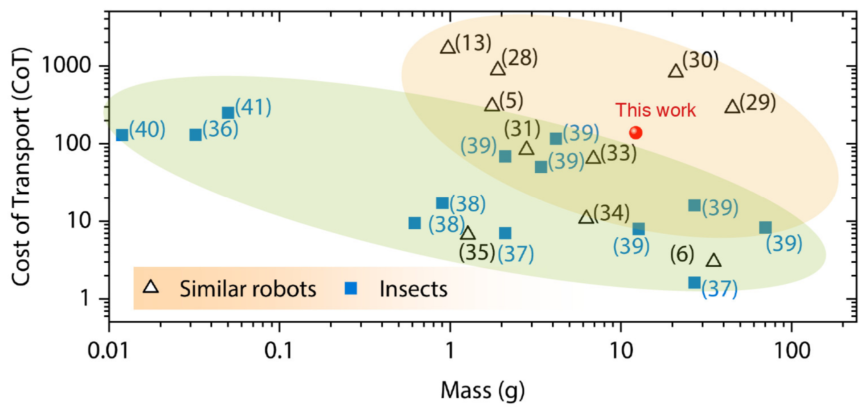

Supplementary Fig. 18.

Comparison of the CoT with insects and similar robots. (Note: Some data are estimated from existing data in their papers.)

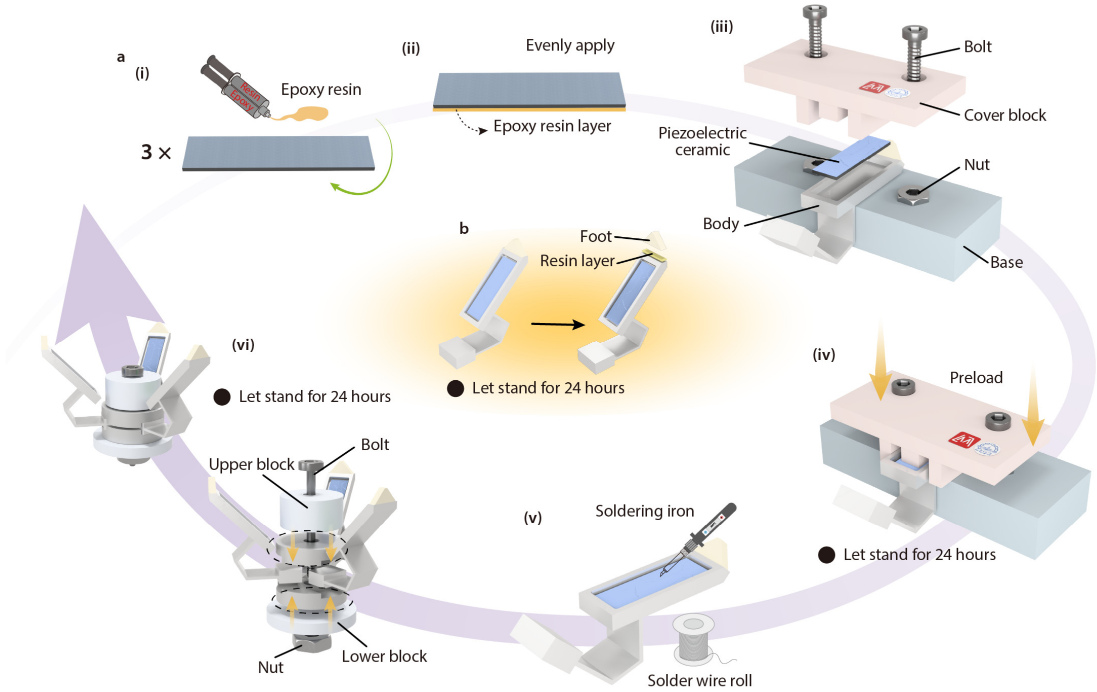

Supplementary Fig. 19.

Fabrication processes of the robot. (a) The fabrication processes. **(b)** The adhesion process of the driving foot.

Table S1. Comparison of key metrics with similar robots.

Actuation mode	Size (cm^3)	Weight (g)	Max. speed (mm/s)/(BL/s)	Min. step (μm)	RC_{min}	DOFs	Endurance
Piezoelectric	Φ3.1×2.75	12.2	30.08 / 0.97	0.56 untethered	1	2	~ 49 min 62.1 m
Piezoelectric[30]	6.3×7.2×1.3	21	0.24 / -	4.06 tethered	1	3	/
Piezoelectric[42]	18.6×18.6×8.7	1282	712 / 3.83	0.49 tethered	1	3	/
Piezoelectric[31,32]	4.5 (length)	2.8	172 / 3.8	~mm scale tethered	>1	2	/
Piezoelectric[28]	2.4 (length)	1.9	28.8 / 1.2	~mm scale untethered	>1	2	~ 19 min
Piezoelectric[43]	4.6×3.6×2.8	34.8	223 / 4.8	0.68 tethered	>1	2	~ 14.5 min
Piezoelectric[29]	5.5×5.5×1.4	45	31.5 / 0.57	~mm scale tethered	1	3	/
Piezoelectric[33]	3×3×1.43	6.9	255 / 8.5	0.25 tethered	>1	2	/
Piezoelectric[44]	2.5×2.5×2.6	1.74	120 / 4.8	~mm scale tethered	>1	2	/
Piezoelectric[34]	5×1×0.15	6.27	302 / 6.04	~mm scale tethered	-	1	/
Piezoelectric[35]	4.35 (length)	1.27	440 / 10.1	~mm scale tethered	>1	2	/
DC motor[5]	2 (length)	1.76	350 / 17.5	~mm scale untethered	>1	2	/
DC motor[6]	7.5×9.5×2.1	35	815 / 10.9	~mm scale untethered	>1	2	~ 25 min
DC motor[7]	10 (length)	16	1500 / 15	~mm scale untethered	>1	2	/
DC motor[8]	6.4 (length)	/	320 / 5	~mm scale tethered	>1	2	/
DC motor[9]	2.5 (length)	1.2	28.3 / 1.1	~mm scale untethered	>1	2	/
Dielectric elastomer[10]	9.1 (length)	/	124 / 1.36 (kV level)	~mm scale tethered	>1	2	/
Dielectric elastomer[11]	10 (length)	9.6	78 / 0.78 (kV level)	~mm scale tethered	>1	2	/
Dielectric elastomer[12]	/	~ 0.62	- / 20.6 (kV level)	~mm scale tethered	-	1	/
Dielectric elastomer[13]	4 (length)	0.97	12 / 0.3 (~ 500V level)	~mm scale untethered	>1	2	~ 15 min

Magnetic[14]	0.9 (length)	0.71	18.9 / 2.1	~mm scale untethered	>1	2	~ 4.5 min
Magnetic[15]	1.5 (length)	0.0455	8 / 0.53	~mm scale limited, magnetic field	-	2	/
Magnetic[16]	0.3 (length)	0.005	213 / -	~mm scale limited, magnetic field	-	2	/
Magnetic[17]	0.8 (length)	/	97.5 / 12.2	~mm scale limited, magnetic field	-	2	/
Shape memory alloy[20]	4.2×0.6×0.4	0.61	0.15 / -	- limited, heating	-	1	/
Shape memory alloy[21]	3 (length)	2.4	30 / 1	~mm scale untethered	>1	2	/

(Note: Some data are estimated from existing data in their paper; priority is given to comparisons involving untethered locomotion data. The degrees of freedom (DOFs) metric primarily focuses on the capability for planar translation along the X and Y axes and rotation about the Z-axis. Notably, single-DOF robots and robots dependent on external magnetic fields are excluded from the RC_{min} evaluation.)